Tight focusing of electromagnetic fields by large-aperture mirrors

D. E. Shipilo,[1,2] I. A. Nikolaeva,[1] V. Yu. Fedorov,[2,3] S. Tzortzakis,[3,4,5] A. Couairon,[6]
N. A. Panov,[1,2] and O. G. Kosareva[1,2,7,*]

[1]*International Laser Center & Faculty of Physics, M. V. Lomonosov Moscow State University, 1/62 Leninskie gori, Moscow 119991, Russia*
[2]*P. N. Lebedev Physical Institute of Russian Academy of Sciences, 53 Leninskiy prospect, Moscow 119991, Russia*
[3]*Science Program, Texas A&M University at Qatar, P.O. Box 23874 Doha, Qatar*
[4]*Institute of Electronic Structure and Laser (IESL), Foundation for Research and Technology—Hellas (FORTH), P.O. Box 1527, GR-71110 Heraklion, Greece*
[5]*Materials Science and Technology Department, University of Crete, 71003 Heraklion, Greece*
[6]*CPHT, CNRS, Ecole Polytechnique, Institut Polytechnique de Paris, Route de Saclay, F-91128 Palaiseau, France*
[7]*Institute of Modern Optics, Nankai University, Tianjin 300350, China*

(Received 3 July 2019; published 25 September 2019)

We derive *nonparaxial input conditions* for simulations of tightly focused electromagnetic fields by means of unidirectional nonparaxial vectorial propagation equations. The derivation is based on the geometrical optics transfer of the incident electric field from significantly curved reflecting surfaces such as parabolic and conical mirrors to the input plane, with consideration of the finite thickness of the focusing element and large convergence angles, making the propagation vectorial and nonparaxial. We have benchmarked numerical solutions of propagation equations initiated with the nonparaxial input conditions against the solutions of Maxwell equations obtained by vectorial diffraction integrals. Both transverse and longitudinal components of the electric field obtained by these methods are in excellent agreement.

DOI: 10.1103/PhysRevE.100.033316

I. INTRODUCTION

From the development of high-power laser chains [1–4] to laser writing in the bulk of optical materials [5] there is a growing need for precisely describing focused electromagnetic fields with large numerical apertures. This requires the solution of Maxwell's equations to correctly describe nonparaxial and vectorial effects in this regime or alternative solutions that reduce the computational cost of Maxwell's solvers, e.g., based on transformation optics [6].

In the linear propagation regime, the solution to Maxwell's equations can be provided by vectorial diffraction integrals (VDIs) [7–10], which generalize the Kirchhoff integral using the Stratton-Chu theory [11]. VDIs naturally describe the propagation of tightly focused radiation using input conditions at the curved surface $z_s(x, y)$ of a focusing element.

The purpose of this work is to describe focused electromagnetic fields using a vectorial unidirectional propagation equation from the focusing element to the focusing point and suitable input conditions that remain valid in the tight-focusing regime. A recent proposal in this direction was to rely on the unidirectional Hertz vector propagation equation (UHPE) [12]:

$$\frac{\partial \widehat{\mathbf{\Pi}}(\omega, k_x, k_y, z)}{\partial z} = ik_z \widehat{\mathbf{\Pi}}(\omega, k_x, k_y, z), \tag{1}$$

where z is the longitudinal (propagation) coordinate, $k_z = \sqrt{k^2(\omega) - k_x^2 - k_y^2}$ is the longitudinal projection of the wave vector $\mathbf{k} = \{k_x, k_y, k_z\}$, the wave number is $k(\omega) = |\mathbf{k}|$, and $\widehat{\mathbf{\Pi}}(\omega, k_x, k_y, z)$ is a spatiotemporal spectrum of the Hertz vector, from which both the electric and the magnetic field vectors can be extracted [13]. Equation (1) describes vectorial and nonparaxial propagation of laser pulses and keeps its validity when nonlinearity sets in [14], at the only additional expense of adding a nonlinear polarization source term describing nonlinear interaction with the medium.

The Hertz vector propagation equation exhibits the universal form of unidirectional propagation equations and thus does not require developing a different solver [15]. It encompasses the unidirectional pulse propagation equation (UPPE) [16] and its generalization the g-UPPE [17], as well as the propagation equation for the vector potential [18,19] in problems where backward-propagating fields can be neglected. The UHPE automatically describes vectorial effects in the linear regime, while the UPPE requires an explicit treatment of this effect.

Simulations of the UHPE, (1), require starting from input conditions, i.e., from the Hertz vector $\widehat{\mathbf{\Pi}}(z = z_0)$ in a plane $z = z_0$ as shown by the explicit solution $\widehat{\mathbf{\Pi}}(z) = \widehat{\mathbf{\Pi}}(z = z_0) \times \exp[ik_z(z - z_0)]$. High-aperture focusing elements usually yield the transmitted or reflected electric field on a surface with significant curvature. Input conditions are then determined by a phase correction to the field that simulates the action of the focusing element. This correction was shown to be limited to beam focusing with low numerical apertures [12]. To overcome this limitation, input conditions for the UHPE were constructed in Ref. [12] by a detailed calculation of diffraction by VDIs from the surface of the optical element to the plane of input conditions $z = z_0$.

*kosareva@physics.msu.ru

Here, we demonstrate that this step can be advantageously replaced by the construction of a suitable input light field distribution for a wide class of optical elements. We verify the validity of this *nonparaxial input condition* by successfully comparing tightly focused electromagnetic fields obtained by the UHPE with the results of the VDI. The proposed approach, based on the geometrical optics transmission of the field from the focusing element surface $z_s(x, y)$ to the plane of input condition $z = 0$, allows us to obtain the analytical corrections of the phase and the amplitude of the incident field.

For an ultrashort broadband pulse propagation the suitable input light field distribution should be found for each harmonic ω of an incident pulse. In this respect our approach is similar to the one used in Ref. [9], where VDIs were applied to find the spatiotemporal light field distribution of a femtosecond pulse in the tight focus of a parabolic mirror.

The advantage of launching the initial light field from the plane $z = 0$ and applying a propagation equation for calculating the light field at a distance $z > 0$ becomes obvious compared with using the VDI if the medium's response is nonlinear. Exactly this situation is relevant for numerous laser-matter interaction studies [20–24]. Adding the nonlinear term in the propagation equation results in the solution of the direct problem consisting in the successive transition of the field in the z direction with a fine step. Using the VDI in a nonlinear medium requires the solution of the inverse problem, as the nonlinear polarization of the medium depends on the light field itself (see Eq. (14) in [11]). Besides, for transmission of the light field from the curved surface to the plane using the VDI the number of operations has a quadratic dependence on the grid size, while for the proposed geometric optics approach the dependence is linear.

II. DERIVATION OF NONPARAXIAL INPUT CONDITIONS FOR NONPARAXIAL PROPAGATION EQUATIONS

A. Requirements for nonparaxial input conditions

In numerical simulations of unidirectional propagation equations where z denotes the propagation axis, the effect of a focusing optical element is usually described by adding a beam curvature to the incident field via a field spatial phase [25],

$$\varphi_p = \gamma k(\omega) z_s(x, y), \tag{2}$$

where γ is a dimensionless coefficient. For a reflective focusing element, $\gamma = 2$ is used in Eq. (2) and $z_s(x, y)$ is a mirror surface. If transmission rather than reflection optics is used, $\gamma = n - 1$ represents the difference between the refractive index of the lens n and that of the surrounding vacuum (or air), and $z_s(x, y)$ is understood as the element thickness along z. The input condition for the propagation equation is then assumed to be defined on the exit surface of the focusing element.

Consider the incident field $\widetilde{\mathbf{E}}_i(\omega, x, y)$, of frequency ω, on a reflecting optical element with a curved surface [see Fig. 1(a)]. After reflection of the incident wave, both the local wave vector and the electric field change their directions. Let us denote the reflected field $\widetilde{\mathbf{E}}_r(\omega, x, y, z_s)$. If focusing is moderate, $\widetilde{\mathbf{E}}_r(\omega, x, y, z_s) = -\widetilde{\mathbf{E}}_i(\omega, x, y, z_s)$ and a paraxial

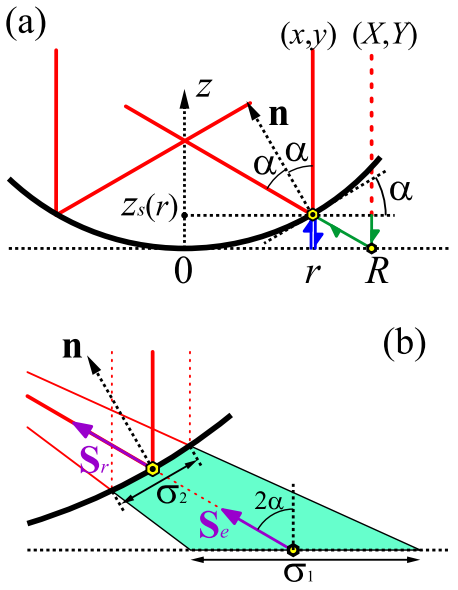

FIG. 1. (a) The geometry of reflection on an axially symmetric optical element. Solid red lines show the incident and reflected rays at an angle α with the normal $\mathbf{n}$ to the mirror at the reflection point $\{r, z_s(r)\}$. Green arrows show the optical path if the reflection point on the mirror surface is replaced by an effective emitter in the plane $z = 0$. Blue arrows show the optical path if the reflection point is projected on the same plane $z = 0$ in the paraxial approximation. (b) Illustration of energy flux conservation in the ray tube (filled); $\mathbf{S}_r$ and $\mathbf{S}_e$ are the Poynting vectors of reflected and emitted waves, respectively.

propagation equation is initiated by the input field,

$$\widetilde{\mathbf{E}}_e(\omega, x, y, z = 0) = \widetilde{\mathbf{E}}_r(\omega, x, y, z_s) e^{i\varphi_p(\omega, x, y)}, \tag{3}$$

defined on the plane $z = 0$, which is assumed to correspond to the exit surface of the focusing element, the thickness of which can be neglected as long as the beam curvature is accounted for in φ_p [25]. This corresponds to the *standard input condition*.

In the case of a high-aperture axially symmetric reflective optical element with a significantly curved surface $z_s(r = \sqrt{x^2 + y^2})$ [see Fig. 1(a)], we look for an input field $\widetilde{\mathbf{E}}_e(\omega, X, Y, 0)$ that can be viewed as being generated by effective emitters located in the plane $z = 0$, which produce exactly the reflected field $\widetilde{\mathbf{E}}_r(\omega, x, y, z_s)$ on the exit surface of the focusing element. Note that X and Y will not necessarily coincide with x and y [see Fig. 1(a)].

During the virtual propagation from $z = 0$ to $z = z_s$, the large beam curvature affects not only the spatial phase but also the amplitude of the input field $\widetilde{\mathbf{E}}_e$. Hence, these fields are linked by an amplitude and phase transformation,

$$\widetilde{\mathbf{E}}_e(\omega, X, Y, z = 0) = \widetilde{\mathbf{E}}_r(\omega, x, y, z_s)\, \Upsilon(r, R)\, e^{i\varphi(\omega, r)}, \tag{4}$$

where $R = \sqrt{X^2 + Y^2}$. Equation (4) encompasses the case of standard input conditions (for optical elements with a low aperture). Indeed, the substitution,

$$X = x, \quad Y = y, \quad R = r, \quad s_e = 2z_s,$$
$$\widetilde{\mathbf{E}}_r = -\widetilde{\mathbf{E}}_i, \quad \Upsilon = 1, \tag{5}$$

makes the nonparaxial input condition, Eq. (4), identical to the standard input condition, Eq. (3). The optical path s_e then corresponds to the blue arrows in Fig. 1(a).

We are looking for expressions for the field amplitude ratio $\Upsilon(r, R)$ and the phase $\varphi(\omega, r) = k(\omega)s_e(r)$, where $s_e(r)$ represents the radius-dependent optical path difference using $r = 0$ as a reference ray as well as the connection between the coordinates $r,\ x,\ y$ and $R,\ X,\ Y$.

Since Eq. (1) is written in the frequency domain, the input condition for a specific field harmonic is obtained in the same way as for a monochromatic beam, therefore we henceforth omit the explicit ω dependence in all fields without loss of generality.

To find the unknown functions in Eq. (4) we apply local geometric optics, which is justified by (i) the high Fresnel number $r^2/(z\lambda) \gtrsim 10^3$, where z is the thickness of the optical element $z_s(r_0)$ at the incident beam edge $r = r_0$, and (ii) the much greater diameter (aperture) of the optical element in comparison with the wavelength $\lambda = 2\pi/k(\omega)$. From additional simulations with the wavelength changed we estimate an applicability threshold of our method as $r_0^2/(z_s(r_0)\lambda) > 50$.

Our goal is to find an analog of Eq. (5) for high-aperture optical elements. Let the angle

$$\alpha(r) = \operatorname{atan}\left(\frac{dz_s}{dr}\right) \tag{6}$$

between the tangent to the reflective surface and the plane $z = 0$ be large. In terms of geometric optics the ray rotates after reflection by the angle 2α relative to the incident one [see Fig. 1(a)], and the electric field of the reflected wave is [7]

$$\widetilde{\mathbf{E}}_r = 2\mathbf{n}(\mathbf{n}\cdot\widetilde{\mathbf{E}}_i) - \widetilde{\mathbf{E}}_i, \tag{7}$$

where $\mathbf{n}$ is the inward surface normal

$$\mathbf{n} = \{n_x, n_y, n_z\} = \frac{\{-\partial z_s/\partial x, -\partial z_s/\partial y, 1\}}{\sqrt{(\partial z_s/\partial x)^2 + (\partial z_s/\partial y)^2 + 1}}. \tag{8}$$

The intersection of the reflected ray with the plane $z = 0$ determines the coordinate of the emission point

$$R(r) = r + z_s(r)\tan 2\alpha(r), \tag{9}$$

where

$$\tan 2\alpha = \frac{2dz_s/dr}{1 - (dz_s/dr)^2}. \tag{10}$$

Equation (9) can be resolved analytically to find $r(R)$ for the surfaces $z_s(r) = Ar^{p/2}$, where A is positive and $p \geqslant 2$ is an integer number. This includes the practical cases of parabolic or conical (reflective axicon [26]) mirrors. The corresponding expressions can be found in Appendix A.

Ray optics is described by the equations [27]

$$\nabla s \cdot \nabla s = 1, \tag{11a}$$

$$\nabla \cdot (|\widetilde{\mathbf{E}}|^2 \nabla s) = 0, \tag{11b}$$

where the eikonal s of the electric field is connected to the phase by $\varphi = ks$ and its increment denotes the optical path of the ray; $|\widetilde{\mathbf{E}}|$ is the amplitude of the electric field. Since the refractive index is uniform and only frequency dependent, we assumed that it is unity in Eq. (11a), while dispersion is fully accounted for via $k(\omega)$ in the propagation equation, (1). Physically, Eq. (11a) describes the trajectory of optical ray, and Eq. (11b) is responsible for the energy flux conservation.

B. Phase correction for nonparaxial input conditions

Let us find the correction of the phase φ in Eq. (4). For this purpose we rewrite Eq. (11a) as $ds = d\xi$, where ξ is the coordinate along a ray. For the incident ray $\xi = -z$. If we calibrate the eikonal of the incident wave to be zero at $z = 0$, it is equal to $s = -z_s(r)$ at the point of reflection $\{x, y, z_s\}$. The eikonal s of the equivalent ray emitted from the point $\{X, Y, 0\}$ to the point $\{x, y, z_s\}$ is $s = \xi - s_e$, where $\xi = z/\cos 2\alpha$ and s_e determines the optical path in Eq. (4). The eikonals of the reflected and equivalent rays should match exactly on their way to focus, including the point $\{x, y, z_s\}$, therefore, one can conclude that

$$s_e(r) = \left(1 + \frac{1}{\cos 2\alpha(r)}\right) z_s(r), \tag{12}$$

where

$$\cos 2\alpha = \frac{1 - (dz_s/dr)^2}{1 + (dz_s/dr)^2}. \tag{13}$$

Note that the transverse component of the wave vector $k_r = k\,ds_e/dR = k\sin 2\alpha$, so the local wave vector points exactly to the reflection point. The optical path s_e determined by Eq. (12) allows the simple geometrical interpretation: the lag of the effective emitted ray is the sum of the distances from the surface $z_s(x, y)$ to the plane $z = 0$ and from the point $\{X, Y, 0\}$ to the point $\{x, y, z_s\}$; see green arrows in Fig. 1(a).

C. Amplitude correction for nonparaxial input conditions

To find the amplitude correction of the emitted field amplitude $|\widetilde{\mathbf{E}}_e(X, Y)|$ with respect to the amplitude of the incident field $|\widetilde{\mathbf{E}}_i(x, y)|$ we integrate Eq. (11b) over the volume Ω of the ray tube [filled area in Fig. 1(b)] bounded by surface Σ using the divergence theorem,

$$\begin{aligned}\int_\Omega \nabla\cdot(|\widetilde{\mathbf{E}}|^2\nabla s)dV &= \oint_\Sigma |\widetilde{\mathbf{E}}|^2(\nabla s\cdot d\boldsymbol{\sigma}) \\ &= |\widetilde{\mathbf{E}}_r|^2\sigma_1\cos\alpha - |\widetilde{\mathbf{E}}_e|^2\sigma_2\cos 2\alpha = 0,\end{aligned} \tag{14}$$

where $\sigma_1 = 2\pi r dr/\cos\alpha$, $\sigma_2 = 2\pi R\,dR$ are the areas of the surfaces bounding the ray tube on the mirror surface $z = z_s(r)$ and plane $z = 0$, respectively. The energy flux through the lateral surface area of the ray tube is zero. Equation (14) can be interpreted as the conservation equation for the electromagnetic energy in the volume Ω, i.e., the flux for the Poynting vector $\mathbf{S} = \varepsilon_0 c(|\widetilde{\mathbf{E}}|^2\nabla s)$ through the surface Σ is zero (ε_0 is the vacuum permittivity). We obtain from Eq. (14) the explicit expression for the correction factor $\Upsilon(r, R) = |\widetilde{\mathbf{E}}_e|/|\widetilde{\mathbf{E}}_r|$ in Eq. (4):

$$\Upsilon(r, R) = \sqrt{\frac{r\,dr}{R\,dR}\frac{1}{\cos 2\alpha}}. \tag{15}$$

D. Construction of nonparaxial input conditions

Nonparaxial input conditions consist in the electric field distribution, (4), the reflected field, (7), the transformation of

coordinates, (9), the phase $\varphi = k\, s_e(r)$ with optical path $s_e(r)$ given by Eq. (12), and the amplitude correction factor, (15). In the limit of small angles $\alpha \to 0$ Eqs. (7), (9), (12), and (15) coincide with the standard input conditions and the paraxial approximation, Eqs. (2) and (3) and (5).

The construction of nonparaxial input conditions from the knowledge of the input field $\widetilde{\mathbf{E}}_i(x, y)$ leads to the definition of $\widetilde{\mathbf{E}}_e(X, Y)$ in five steps:

1. Definition of the spatial grid (X, Y) for the propagation solver.
2. Mapping of (X, Y) onto (x, y) in the following way: $\{x = Xr/R,\ y = Yr/R\}$, with $R = \sqrt{X^2 + Y^2}$ and r obtained by solving Eq. (9) analytically or numerically.
3. Calculation of the field phase $\varphi(r(R)) = ks_e(r(R))$ and amplitude correction $\Upsilon(r, R)$ according to Eqs. (12) and (15).
4. Calculation of the reflected field $\widetilde{\mathbf{E}}_r(x, y)$ according to Eq. (7).
5. Calculation of the field $\widetilde{\mathbf{E}}_e(X, Y)$ according to Eq. (4).

The field distribution $\widetilde{\mathbf{E}}_e(X, Y)$ is then Fourier-transformed and its initial angular spectrum $\widehat{\mathbf{E}}(k_x, k_y)$ is transformed to an input Hertz vector spectrum according to Eq. (B4) and provided to the solver for propagation Eq. (1). Applying discrete Fourier transformation in simulations assumes periodicity of the light field in both spatial (k-vector) and temporal (frequency) domains. Tight focusing is typically considered for the beam distribution with the maximum on-axis intensity and zero boundary conditions in space and time. Mathematically required periodicity should be ensured by a light field distribution in the center of the solver grid surrounded by a large zero buffer zone in all the domains.

The time required for this routine is proportional to the number of nodes $N_x \times N_y$. Had the input field been reconstructed using VDIs, $\propto N_x^2 \times N_y^2$ operations would have been required, because the value of the field $\widetilde{\mathbf{E}}_e(X, Y)$ at each node of the two-dimensional grid is obtained as an integral over the mirror surface [9].

III. SIMULATIONS OF FOCUSING USING NONPARAXIAL INPUT CONDITIONS

Numerical simulations were performed with the UHPE, (1), initiated by nonparaxial input conditions to propagate tightly focused beams from the mirror plane to the focal plane. Referring to frequently used experimental or numerical focusing conditions we use a top-hat monochromatic beam at the wavelength of 800 nm and a large numerical aperture [1,6,28],

$$\widetilde{\mathbf{E}}_i(r) = \mathbf{e}_x E_0 \exp\left(-\frac{r^{16}}{r_0^{16}}\right), \tag{16}$$

where $r_0 = 1$ mm is the beam radius.

First, we study focusing by the parabolic mirror

$$z_s(r) = \frac{r^2}{4f} \tag{17}$$

in the case of moderate focusing and assume the focal length $f \approx 3$ mm [f-number $= 0.5/\tan 2\alpha(r_0) = 1.5$ and numerical aperture NA $= \sin 2\alpha(r_0) = 0.33$], for which the paraxial input, (3), is not suitable [12]. Therefore, we calculate the input field $\widetilde{\mathbf{E}}_e$ from Eq. (4) and its spectrum $\widehat{\mathbf{E}}_e$. The corresponding input Hertz vector is calculated according to the procedure described in Appendix B, Eq. (B4). After propagation, the electric field components are reconstructed from the Hertz vector as indicated in Appendix B, Eq. (B1).

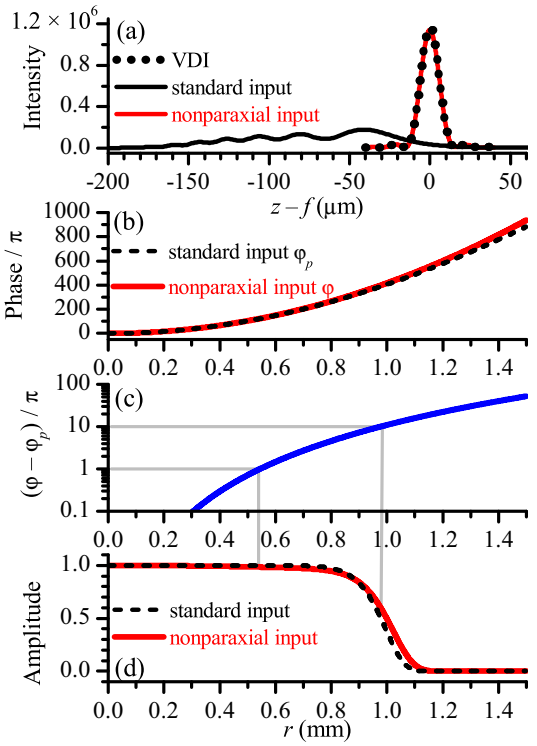

FIG. 2. Focusing by the parabolic mirror with the focal length $f \approx 3$ mm ($f/1.5$, NA $= 0.33$). (a) Variation of $|E_x|^2$ on the beam axis $r = 0$ with propagation distance z calculated by the UHPE with paraxial or standard (solid black curve) and nonparaxial input conditions (red curve). Comparison is made with vectorial diffraction integrals (black dots). (b) Phase and (d) amplitude of standard (dashed curve) and nonparaxial (solid curve) input conditions. (c) The log-scaled difference between nonparaxial φ and standard φ_p phases.

Figure 2(a) shows the on-axis intensity of the x component of the electric field as a function of the propagation distance z. For the sake of comparison, propagation is initiated with standard or nonparaxial input conditions and results are confronted with the results obtained with VDI. Our correction to the input field provides results in excellent agreement with the intensity distribution obtained from VDI while the standard input condition fails to reproduce it.

A comparison of the phase and amplitude of the electric field at the initial plane $z = 0$ for standard, (2) and (5), and nonparaxial input conditions is shown in Figs. 2(b)–2(d). Both the phase difference and the amplitude difference do not seem significant, however, the phase difference crucially influences the field propagation. The phase difference between nonparaxial and paraxial inputs $\varphi - \varphi_p$ reaches π at $r \approx 0.55$ mm, where the field amplitude is about unity [see Fig. 2(c)]. A phase difference of 10π at $r \approx 1$ mm corresponds to a field amplitude of 0.5 [trace gray line from Fig. 2(c) to Fig. 2(d)]. This is enough to make the standard input

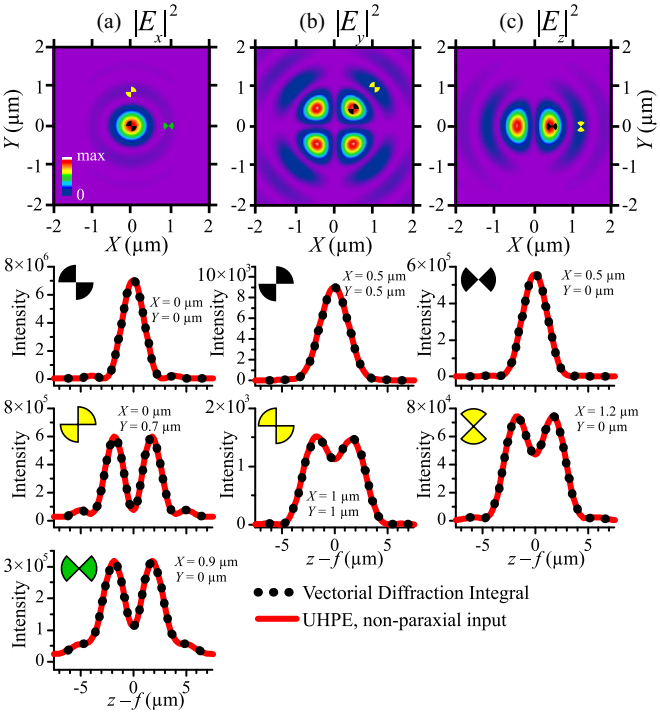

FIG. 3. Focusing of the beam, (16), by the parabolic mirror, (17), with the focal length $f \approx 1.2$ mm ($f/0.6$, NA $= 0.64$). The transverse (X, Y) distributions of (a) $|E_x|^2$, (b) $|E_y|^2$, and (c) $|E_z|^2$ in the focus (upper row; in each panel the squared modulus of the field is normalized by its maximum value). Marked panels show the longitudinal distributions with propagation distance z of the quantities $|E_x|^2$ (left column), $|E_y|^2$ (middle column), and $|E_z|^2$ (right column) in the transverse positions indicated by the corresponding markers in the upper row. Simulation results are obtained from the UHPE with nonparaxial input conditions (solid curve) and the VDI (dots).

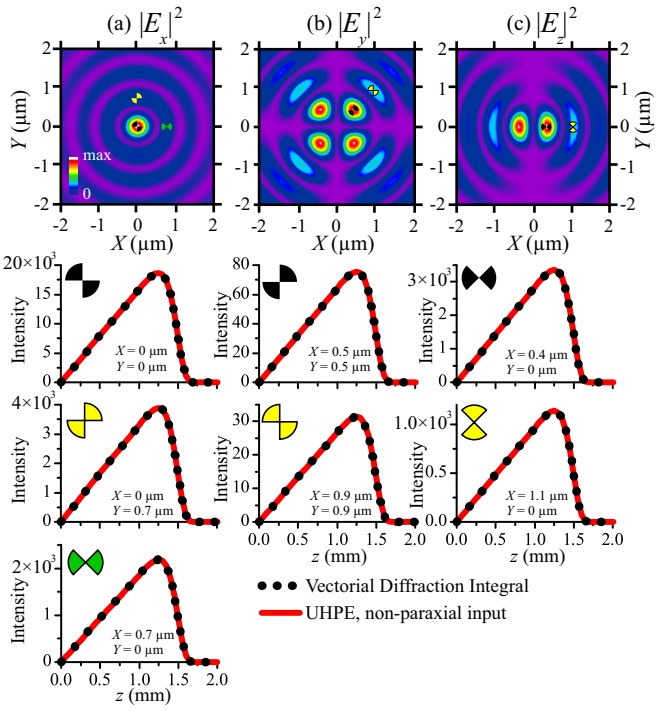

FIG. 4. Same as Fig. 3, for the propagation after reflection from a conical mirror, (18), with angle $\alpha = 20^\circ$ ($f/0.6$, NA $= 0.64$). The upper row corresponds to $z = 1.26$ mm.

condition insufficiently accurate to describe focusing under these conditions.

For NA $= 0.33$ vectorial effects are not significant yet. This means that the amplitude correction can be relaxed. We obtained almost the same results as in Fig. 2(a) by using the scalar unidirectional pulse propagation equation with axial symmetry, initiated with a relaxed nonparaxial input condition, i.e., a nonparaxial input condition with $\widetilde{\mathbf{E}}_r = -\widetilde{\mathbf{E}}_i$ instead of Eq. (7).

We consider the case of tighter focusing of the beam, (16), by a parabolic mirror with focal length $f \approx 1.2$ mm (f-number $= 0.6$ and NA $= 0.64$). Intensity patterns in the focus and profiles along the propagation distance are shown in Fig. 3 for the three components of $|E_\eta|^2$, where $\eta = x, y, z$. These intensity distributions are typical for such focusing conditions [7,9,12,18,23]. We found excellent agreement between the profiles obtained by propagation using the UHPE with nonparaxial input conditions (red curve) and their counterparts obtained by vectorial diffraction integrals (dotted black curve), both for the beam center and for the periphery. Thus, the UHPE with nonparaxial input conditions allowed us to simulate the propagation of all components of the electric fields under tight focusing conditions, in agreement with the results of vectorial diffraction integrals.

The aforementioned procedure is valid for a wide class of reflective focusing elements. As a benchmark for focusing by the parabolic mirror we used the VDI derived by Varga and Török [7]. Following their derivation, we ensured that this form of the VDI can be applied for an arbitrary surface $z_s(x, y)$, if one uses the corresponding expression for the inward surface normal, (8), through all the formulas.

Figure 4 shows the the results of simulations for the focusing by a conical mirror,

$$z_s = r \tan \alpha, \tag{18}$$

where the angle $\alpha = 20^\circ$ between the plane $z = 0$ and the mirror yields f-number $= 0.6$, NA $= 0.64$. The transverse distributions of x and z components of the field (Fig. 4; upper row) look similar to the ones measured and calculated in the literature [29,30]. The intensity distribution at the focus of the conical mirror exhibits the typical quasi-Bessel beam pattern obtained by axicon focusing [31]. Energy is weakly localized, in contrast with the focal spot of the parabolic mirror (cf. Fig. 3 with Fig. 4). As a result, each component of the electric field is an order of magnitude lower for the conical mirror than for the parabolic one.

The results of our numerical simulations of beam focusing by a conical mirror based on the UHPE with nonparaxial input conditions reproduce well the features of axicon focusing appearing in small angle axicons [32,33]. For example, the linear dependence of the on-axis intensity on the propagation distance shown in the profiles in Fig. 4 was simulated and explained in terms of geometrical optics [33].

In order to generalize the results, we study the focusing by a mirror of surface $z_s(r)$ that does not lead to an analytic

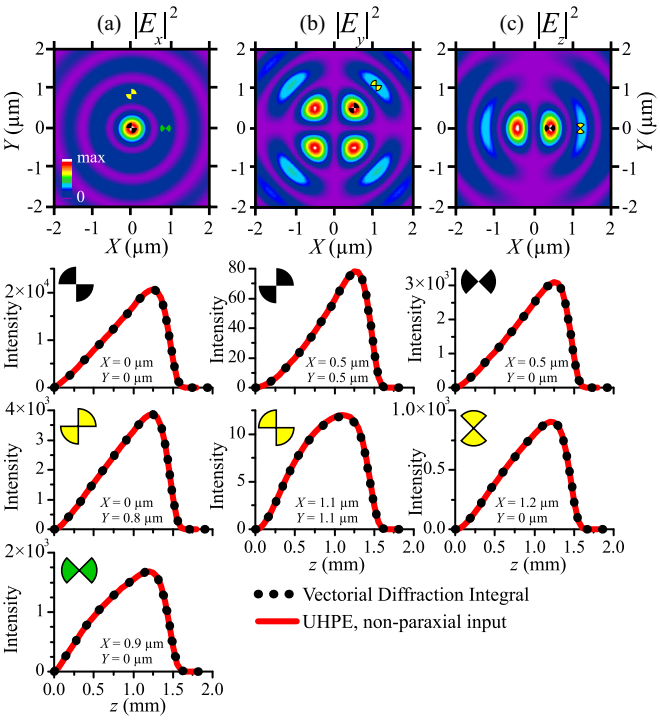

FIG. 5. Same as Fig. 3, for the propagation after reflection from the mirror $z_s \propto r^{1.1}$ ($f/0.6$, NA $= 0.64$). The upper row corresponds to $z = 1.195$ mm.

solution of Eq. (9), in contrast with the parabolic or the conical mirrors. The mirror surface is given by

$$z_s \propto r^{1.1} \tag{19}$$

with effective f-number $= 0.6$, NA $= 0.64$ (the same as in the previous cases).

The dependence $r(R)$ was found numerically from Eq. (9) as well as the derivatives in Eqs. (6), (8), and (15). Figure 5 shows intensity patterns at focus and intensity profiles along the propagation axis in comparison with the results of diffraction integrals. The excellent agreement between the UHPE solution with nonparaxial input conditions and the VDI (Fig. 5) evidences the applicability of the input conditions for general optical elements.

Thus, the method developed for the simulations of beam focusing by unidirectional nonparaxial vectorial propagation equations is fully benchmarked, as it shows that the intensity distributions found from the UHPE and VDI match, validating our method to construct nonparaxial input conditions. Repeating the routine of building the Hertz vector for every harmonic ω in a broadband spectrum of an ultrashort pulse and taking the Fourier transform in time, one can obtain an (x, y, z) distribution of electric and magnetic fields at any given instant in time, which can be used as initial conditions for finite-difference time-domain [34] or particle-in-cell [35] simulations in the focal volume.

IV. CONCLUSIONS

In conclusion, we have derived input conditions compatible with unidirectional nonparaxial vectorial propagation equations. We used geometrical optics to transfer the field from a curved focusing surface to the plane of input conditions for the unidirectional Hertz vector propagation equation. With respect to standard input conditions, both the phase and the amplitude must be modified in the case of nonparaxial vectorial propagation. The solutions to the propagation equation initiated by the nonparaxial input condition are consistent with exact solutions of Maxwell equations calculated by vectorial diffraction integrals for the three components of the field and a wide class of focusing surfaces.

The results can be, in principle, applied to transmission optics, because the main approximations used (high Fresnel number for propagation through the focusing element and absence of ray intersection) will be held as well. In this case, the only change required in our procedure involves the rotation of the wave vectors that must satisfy Snell's law and the rotation of the field vectors by Fresnel's equations.

ACKNOWLEDGMENTS

This work was performed in the framework of the FIR-LAB International Research Network. We are grateful for the financial support from the Russian Foundation for Basic Research (Grants No. 18-52-16020, No. 18-32-01000, and No. 18-02-00954), "Basis" Foundation, Scholarship of the Russian Federation President (Grant No. SP-2453.2018.2), and National Key Research and Development Program (Grant No. 2018YFB0504400). We also acknowledge support from National Priorities Research Program Grant No. NPRP9-383-1-083 of the Qatar National Research Fund (member of The Qatar Foundation).

APPENDIX A: NONPARAXIAL INPUT CONDITIONS FOR VECTORIAL PROPAGATION EQUATIONS IN THE CASE OF FOCUSING BY AXIALLY SYMMETRIC LARGE-APERTURE PARABOLIC AND CONICAL MIRRORS

Since beam focusing by the parabolic, (17), and conical, (18), mirrors are of the most practical importance, we write out explicitly nonparaxial input conditions in these cases. The incident electric field is assumed to be linearly polarized along the x axis $\widetilde{\mathbf{E}}_i = \{E_0(x, y), 0, 0\}$. The transverse grids $\{X, Y\}$ on the plane $z = 0$ and $\{x, y\}$ on the mirror $z_s(x, y)$ are connected by $x = Xr/R$, $y = Yr/R$, where $r = \sqrt{x^2 + y^2}$, $R = \sqrt{X^2 + Y^2}$, and the dependence $r(R)$ is given by the solution of Eq. (9).

For a parabolic mirror of focal length f, the initial electric field distribution for a harmonic of frequency ω with the wave number k can be written as

$$\widetilde{\mathbf{E}}_e(X, Y, z = 0) = E_0(x, y)\,\frac{4f^2 - r^2}{4f^2 + r^2}\left\{\left(\frac{x^2 - y^2}{4f^2} - 1\right)\mathbf{e}_x + \frac{xy}{2f^2}\mathbf{e}_y - \frac{x}{f}\mathbf{e}_z\right\}\exp\left(i\frac{2k\,r^2 f}{4f^2 - r^2}\right), \tag{A1}$$

where the coordinate of the reflection point is

$$r(R) = \frac{2f}{R}(\sqrt{f^2 + R^2} - f). \tag{A2}$$

Similar equations are obtained for a conical mirror of angle α between the reflecting surface and the plane $z = 0$,

$$\begin{aligned}\widetilde{\mathbf{E}}_e(X, Y, z = 0) &= E_0(x, y)\cos^2\alpha\sqrt{\cos 2\alpha}\left\{\left(\frac{x^2 - y^2}{r^2}\tan^2\alpha - 1\right)\mathbf{e}_x \right. \\ &\left. + \frac{2xy}{r^2}\tan^2\alpha\,\mathbf{e}_y - \frac{2x}{r}\tan\alpha\,\mathbf{e}_z\right\}\exp\left(i\,k\,r\,\tan 2\alpha\right),\end{aligned} \tag{A3}$$

and the coordinate of the reflection point is

$$r(R) = R\cos 2\alpha. \tag{A4}$$

APPENDIX B: ELECTRIC FIELD–TO–HERTZ VECTOR TRANSFORMATION

In our simulations we used the UHPE, Eq. (1), a vectorial nonparaxial propagation equation for the Hertz vector $\mathbf{\Pi}$. In general, the Hertz vector $\mathbf{\Pi}$ is three-dimensional, and the electric field $\mathbf{E}$ is obtained from $\mathbf{\Pi}$ by the relation

$$\mathbf{E} = -\frac{1}{c^2}\frac{\partial^2\mathbf{\Pi}}{\partial t^2} + \nabla(\nabla\cdot\mathbf{\Pi}), \tag{B1}$$

where c is the speed of light in vacuum. The spectral components of $\mathbf{E}$ and $\mathbf{\Pi}$ obtained after Fourier transformation in time and transverse directions from (t, x, y, z) to (ω, k_x, k_y, z) satisfy

$$\widehat{\mathbf{E}}(\omega, k_x, k_y, z) = C\widehat{\mathbf{\Pi}}(\omega, k_x, k_y, z), \tag{B2}$$

where the matrix C is

$$C = \begin{pmatrix} k^2(\omega) - k_x^2 & -k_xk_y & -k_xk_z \\ -k_yk_x & k^2(\omega) - k_y^2 & -k_yk_z \\ -k_zk_x & -k_zk_y & k^2(\omega) - k_z^2 \end{pmatrix} \tag{B3}$$

and k_z is expressed via ω, k_x, and k_y as $k_z = \sqrt{k^2(\omega) - k_x^2 - k_y^2}$. The matrix, (B3), represents a spectral operator that cannot be inverted. This is due to the fact that the Hertz vector, as for other electromagnetic potentials, can be chosen so as to follow an additional gauge condition, which amounts to selecting only two components for the Hertz vector, from which the three components of the electric field can be retrieved. We therefore require $\Pi_z = 0$ as in Ref. [12], and only two components of the electric field must be chosen so as to calculate the components of the Hertz vector $\mathbf{\Pi} = \{\Pi_x, \Pi_y\}$. The third component of the field, calculated according to Eq. (B1), automatically satisfies the equation $(\nabla\cdot\mathbf{E}) = 0$.

Our results were obtained by using the inverse transform from the field $\mathbf{E}$ to the Hertz vector $\mathbf{\Pi}$ using the main two components for the field $\{E_x, E_z\}$ and the two nonzero components of the Hertz vector $\{\Pi_x, \Pi_y\}$:

$$\begin{pmatrix}\widehat{\Pi}_x \\ \widehat{\Pi}_y\end{pmatrix} = \frac{1}{k^2(\omega)k_zk_y}\begin{pmatrix}-k_yk_z & k_xk_y \\ k_xk_z & k^2(\omega) - k_x^2\end{pmatrix}\begin{pmatrix}\widehat{E}_x \\ \widehat{E}_z\end{pmatrix}. \tag{B4}$$

The third field component E_y was obtained from the corresponding component of Eq. (B1).

[1] T. M. Jeong and J. Lee, Ann. Phys. (Berlin) **526**, 157 (2014).
[2] D. N. Papadopoulos, P. Ramirez, K. Genevrier, L. Ranc, N. Lebas, A. Pellegrina, C. L. Blanc, P. Monot, L. Martin, J. P. Zou, F. Mathieu, P. Audebert, P. Georges, and F. Druon, Opt. Lett. **42**, 3530 (2017).
[3] P. Lassonde, S. Mironov, S. Fourmaux, S. Payeur, E. Khazanov, A. Sergeev, J.-C. Kieffer, and G. Mourou, Las. Phys. Lett. **13**, 075401 (2016).
[4] G. Fibich, Y. Sivan, Y. Ehrlich, E. Louzon, M. Fraenkel, S. Eisenmann, Y. Katzir, and A. Zigler, Opt. Express **14**, 4946 (2006).
[5] R. Drevinskas, J. Zhang, M. Beresna, M. Gecevičius, A. G. Kazanskii, Y. P. Svirko, and P. G. Kazansky, Appl. Phys. Lett. **108**, 221107 (2016).
[6] M. Chanal, V. Y. Fedorov, M. Chambonneau, R. Clady, S. Tzortzakis, and D. Grojo, Nat. Commun. **8**, 773 (2017).
[7] P. Varga and P. Török, J. Opt. Soc. Am. A **17**, 2081 (2000).
[8] M. J. Nasse and J. C. Woehl, J. Opt. Soc. Am. A **27**, 295 (2010).
[9] T. M. Jeong, S. Weber, B. Le Garrec, D. Margarone, T. Mocek, and G. Korn, Opt. Express **23**, 11641 (2015).
[10] X. Zeng and X. Chen, Opt. Express **27**, 1179 (2019).
[11] J. A. Stratton and L. Chu, Phys. Rev. **56**, 99 (1939).
[12] A. Couairon, O. G. Kosareva, N. A. Panov, D. E. Shipilo, V. A. Andreeva, V. Jukna, and F. Nesa, Opt. Express **23**, 31240 (2015).
[13] E. A. Essex, Am. J. Phys. **45**, 1099 (1977).
[14] C. S. Milsted and C. D. Cantrell, Phys. Rev. A **53**, 3536 (1996).
[15] A. Couairon, E. Brambilla, T. Corti, D. Majus, O. de J. Ramírez-Góngora, and M. Kolesik, Eur. Phys. J. Spec. Top. **199**, 5 (2011).
[16] M. Kolesik and J. V. Moloney, Phys. Rev. E **70**, 036604 (2004).
[17] J. Andreasen and M. Kolesik, Phys. Rev. E **86**, 036706 (2012).
[18] S. G. Bochkarev and V. Y. Bychenkov, Quant. Electron. **37**, 273 (2007).
[19] P. Mora and T. M. Antonsen, Jr., Phys. Plasmas **4**, 217 (1997).
[20] C. Arnold, A. Heisterkamp, W. Ertmer, and H. Lubatschowski, Opt. Express **15**, 10303 (2007).
[21] V. A. Andreeva, O. G. Kosareva, N. A. Panov, D. E. Shipilo, P. M. Solyankin, M. N. Esaulkov, P. G. de Alaiza Martínez, A. P. Shkurinov, V. A. Makarov, L. Bergé *et al.*, Phys. Rev. Lett. **116**, 063902 (2016).
[22] V. Y. Fedorov, M. Chanal, D. Grojo, and S. Tzortzakis, Phys. Rev. Lett. **117**, 043902 (2016).
[23] P. González de Alaiza Martínez, G. Duchateau, B. Chimier, R. Nuter, I. Thiele, S. Skupin, and V. T. Tikhonchuk, Phys. Rev. A **98**, 043849 (2018).
[24] G. Fibich and B. Ilan, Physica D (Amsterdam) **157**, 112 (2001).
[25] J. W. Goodman, *Introduction to Fourier Optics* (Roberts and Company, Devon, UK, 2005).

[26] J. H. McLeod, J. Opt. Soc. Am. **44**, 592 (1954).
[27] M. Born and E. Wolf, *Principles of Optics: Electromagnetic Theory of Propagation, Interference and Diffraction of Light* (Elsevier, Amsterdam, 2013).
[28] H. Kiriyama, A. S. Pirozhkov, M. Nishiuchi, Y. Fukuda, K. Ogura, A. Sagisaka, Y. Miyasaka, M. Mori, H. Sakaki, N. P. Dover *et al.*, Opt. Lett. **43**, 2595 (2018).
[29] R. Arimoto, C. Saloma, T. Tanaka, and S. Kawata, Appl. Opt. **31**, 6653 (1992).
[30] S. N. Khonina, S. V. Karpeev, S. V. Alferov, D. A. Savelyev, J. Laukkanen, and J. Turunen, J. Opt. **15**, 085704 (2013).
[31] J. Durnin, J. J. Miceli, Jr., and J. H. Eberly, Phys. Rev. Lett. **58**, 1499 (1987).
[32] P. Polesana, D. Faccio, P. Di Trapani, A. Dubietis, A. Piskarskas, A. Couairon, and M. A. Porras, Opt. Express **13**, 6160 (2005).
[33] S. Y. Popov and A. T. Friberg, Opt. Eng. **34**, 2567 (1995).
[34] K. Yee, IEEE Trans. Antennas Propag. **14**, 302 (1966).
[35] J. M. Dawson, Rev. Mod. Phys. **55**, 403 (1983).